

Research Article

Synthesis and Characterization of ZnO-ZrO₂ Nanocomposites for Photocatalytic Degradation and Mineralization of Phenol

M. C. Uribe López,¹ M. A. Alvarez Lemus^{ID, 1}, M. C. Hidalgo,² R. López González^{ID, 1}, P. Quintana Owen,³ S. Oros-Ruiz,⁴ S. A. Uribe López,⁵ and J. Acosta¹

¹Juárez Autonomous University of Tabasco, Nanotechnology for Biomedicine and Environmental Applications, Academic Division of Engineering and Architecture, Carr. Cunduacán Jalpa de Méndez Km 1, Col. La Esmeralda, CP 86690 Cunduacan, Tabasco, Mexico

²Instituto de Ciencia de Materiales de Sevilla (ICMS), Consejo Superior de Investigaciones Científicas (CSIC)-Universidad de Sevilla, Américo Vespucio 49, 41092 Sevilla, Spain

³CINVESTAV Unidad Mérida, Departamento de Física Aplicada, AP. 73 Cordemex, 97310 Mérida, Yucatán, Mexico

⁴Autonomous Metropolitan University-Iztapalapa, CONACYT-Research Fellow-Department of Chemistry, ECOCATAL Group, Av. San Rafael Atlixco No. 186, Col. Vicentina, Iztapalapa 09340, Mexico

⁵Juárez Autonomous University of Tabasco, CONACYT-Research Fellow, Academic Division of Engineering and Architecture, Carr. Cunduacán Jalpa de Méndez Km 1, Col. La Esmeralda, CP 86690 Cunduacan, Tabasco, Mexico

Correspondence should be addressed to M. A. Alvarez Lemus; mayra.alvarez@ujat.mx

Received 18 June 2018; Revised 8 October 2018; Accepted 1 November 2018; Published 10 January 2019

Guest Editor: Zhen Yu

Copyright © 2019 M. C. Uribe López et al. This is an open access article distributed under the Creative Commons Attribution License, which permits unrestricted use, distribution, and reproduction in any medium, provided the original work is properly cited.

ZnO-ZrO₂ nanocomposites using zinc (II) acetylacetone and different ZnO contents (13, 25, 50, and 75% mol) were synthesized through sol-gel method. The synthesis process was strongly related to nanocomposite properties especially on their structural composition. The obtained ZnO-ZrO₂ nanomaterials presented tetragonal crystalline structure for zirconia whereas hexagonal one was formed in ZnO. Raman spectroscopy and XRD patterns confirmed the formation of tetragonal zirconia whereas inhibition of monoclinic structure was observed. Addition of ZnO affected the pore size distribution of the composite, and the measured specific surface areas were from 10 m²/g (for pure ZnO) to 46 m²/g (pristine ZrO₂). Eg values of ZrO₂ were modified by ZnO addition, since calculated values using Kubelka-Munk's function varied from 4.73 to 3.76 eV. The morphology and size of the nanomaterials investigated by electron microscopy showed formation of nanorods for ZnO with sizes ranging from 50 nm to 300 nm while zirconia was formed by smaller particles (less than 50 nm). The main advantage of using the nanocomposite for photocatalytic degradation of phenol was the mineralization degree, since 75ZnO-ZrO₂ nanocomposite surpassed mineralization reached by pure ZnO and also inhibited formation of undesirable intermediates.

1. Introduction

Zirconium oxide (ZrO₂) known as zirconia is an interesting material due to its application in various photochemical heterogeneous reactions. ZrO₂ is an n-type semiconductor with a wide band gap energy between 5.0 and 5.5 eV [1]. Because of this, ZrO₂ requires UV-C light (<280 nm) to be excited and generate electron-hole pairs [2]. A strategy to overcome this is by doping ZrO₂ with different transition metal ions or coupling with other metal oxides with dissimilar band edge [3]. Composites made of two metal oxides have attracted much attention in different researches because they possess

improved physicochemical properties than the pure oxides. Usually, composites enhance photocatalytic activity [4, 5], produce new crystallographic phases with quite different properties than the original oxides, create defect energy levels in the band gap region [6], change the surface characteristics of the individual oxides due to the formation of new sites in the interface between the components [7], and also increase the stability of a photoactive crystalline phase [8]. In order to enhance optical properties of ZrO₂ several semiconductors like SiO₂, TiO₂, ZnO, WO₃, and NiO have been coupled to ZrO₂. Together with TiO₂, zinc oxide is one of the most investigated n-type semiconductor materials due to its low-cost,

easy fabrication, wide band-gap, and photocatalytic activity for degrading several organic pollutants into less harmful products [9]. The main advantage of ZnO is that it absorbs a larger fraction of the solar spectrum than TiO₂ [10]. The band gap of ZnO is ~3.37 eV, and its exciton-binding energy is about 60 meV [11]. Many reports have been published about the good physicochemical properties given by the use of ZnO in composites. For instance, a composite made by nanostructures transparent conducting metal-oxides (TCMOS) as ZnO/NiO resulted in an excellent candidate for acetone sensing [12]. Nanocomposites of Zn(1-x)MgxO/graphene showed an excellent performance to remove methylene blue dye under natural sunlight illumination [13]. TiO₂/ZnO nanocomposites with different contents of ZnO showed an improvement in the degradation of the organic dyes brilliant green and methylene blue under solar light irradiation [14]. ZnO/TiO₂ photocatalyst exhibited much higher photocatalytic activity than pure TiO₂, ZnO, and P-25 in the degradation of 4-chlorophenol under low UV irradiation [15]. The composites of ZnO/Ag₂CO₃/Ag₂O demonstrated a potential effect in the photodegradation of phenol under visible light irradiation due to the facilitate charge transfer and suppress recombination of photogenerated electrons and holes [16].

Recently, composites of ZrO₂ with ZnO have attracted much attention because of their excellent properties as a semiconductor material, especially for the degradation reactions of recalcitrant organic pollutants. The enhancement in photocatalytic activity of ZnO-ZrO₂ composites has been associated with the changes in their structural, textural, and optical properties, such as surface area, particle size, formation of a specific crystalline phase, and low band gap energy [4, 17, 18]. In addition, the improved electron-hole pair enhances the photocatalytic efficiency. Under illumination, both the semiconductors of nanocomposite are simultaneously excited, and the electrons slip to the low-lying conduction band of one semiconductor, while holes move to the less anodic valence band. Sherly et al. [19] attributed the efficiency of Zn₂Zr (ZnO and ZrO₂ in 2:1 ratio) photocatalyst in the degradation of 2,4-dichlorophenol to the good stability and the efficient separation of photogenerated electron-hole pairs. Aghabeygi and Khademi-Shamami [4] stated that the good properties of 1:2 molar ratio of ZrO₂:ZnO as photocatalyst in the degradation of Congo Red dye could be by the decrease in the rate of the hole-electron pairs recombination when the excitation takes place with energy lower than E_g. Besides, they proposed that ZnO could increase the concentration of free electrons in the CB of ZrO₂ by reducing the charge recombination in the process of electron transport. Gurushantha et al. [20] demonstrated a photocatalytic enhancement in the ZrO₂/ZnO (1:2) nanocomposite for the degradation of acid orange 8 dye under UV light irradiation (254 nm). They observed that the reduction of energy gap, the increase of the density states, and the stability of the composite increased the photocatalyst efficiency.

In this work, we investigated the effect of ZnO on the photocatalytic properties of ZnO-ZrO₂ nanocomposites obtained by sol-gel method in the photodegradation of phenol in water under UV-A irradiation.

2. Materials and Methods

2.1. Reagents. Zirconium (IV) butoxide (80 wt. % in 1-butanol), phenol (ReagentPlus ≥99%), and Zinc Acetylacetone hydrate were purchased from Sigma-Aldrich; hydrochloric acid (36.5–38%) was obtained from Civeq (México). In all cases, deionized water was used.

2.2. Synthesis of ZrO₂. 81.2 mmol of Zirconium (IV) butoxide were added dropwise to 48.9 mL of deionized water and ethanol mixture (1:8) preheated at 70°C. Before addition of the alkoxide, pH was adjusted at pH 3 with hydrochloric acid (2.5 M). The white suspension was kept under temperature at 70°C, with continuous stirring and reflux for 24 h. The gel was dried at 70°C for 8 h afterwards. Finally, the obtained powder was ground and then calcined at 500°C for 4 h.

2.3. Synthesis of ZnO. 11.38 mmol of Zinc Acetylacetone hydrate (powder, Sigma-Aldrich) were added into 50 mL of ethanol (96%, Civeq) previously heated at 70°C and adjusted at pH 3 with chlorhydric acid (2.5 M) (36.5–38%, Civeq) during 30 min. The suspension was stirred for 4 h at 70°C and then being aged for 24 h under continuous agitation. Later, the resulting gel was washed several times with ethanol and deionized water. Finally, the white powders were dried at 70°C during 6 h, ground, and then calcined at 500°C for 4 h.

2.4. Synthesis of ZnO-ZrO₂ Nanocomposites. Different molar percentages (13%, 25%, 50%, and 75%) of ZnO were incorporated into ZrO₂ and named as 13ZnO-ZrO₂, 25ZnO-ZrO₂, 50ZnO-ZrO₂, and 75ZnO-ZrO₂. The photocatalysts were prepared as follows: the appropriated amount of Zinc Acetylacetone hydrate was dissolved into 50 mL of ethanol previously heated at 70°C and adjusted at pH 3 (HCl, 2.5 M). ZrO₂ sols were prepared separately as previously described but just before the addition of the half of the total amount of alkoxide was completed, the corresponding ZnO sol was incorporated into the mixture, followed by the dropwise of the rest of the zirconium alkoxide. The mixture was kept under vigorous stirring and reflux at 70°C during 24 h. The obtained gels were washed several times with ethanol and deionized water, then they were, dried, ground, and calcined at 500°C during 4 h. The proposed reactions are presented in Supplementary Materials (Figures S1, S2, and S3).

2.5. Characterization of the Nanocomposites. X-ray diffraction (XRD) patterns were obtained on a Bruker D8 Advance diffractometer using CuKα radiation (1.5418 Å) in the 2θ scan range of 10–90°. The average crystallite size of the samples was estimated using the Debye-Scherrer equation (equation (1)).

$$D = \frac{0.89\lambda}{\beta \cos \theta}, \quad (1)$$

where λ is the wavelength of CuKα radiation, β is the peak width at half maximum, and θ is the diffraction angle.

To calculate the percentage of monoclinic and tetragonal phases of pure ZrO_2 , we used the monoclinic phase fraction X_m and the following equation described by Garvie and Nicholson [21]:

$$X_m = \frac{I_{m(-111)} + I_{m(111)}}{I_{m(-111)} + I_{m(111)} + I_{t(101)}} \times 100, \quad (2)$$

where I_m and I_t represent the integral intensities of monoclinic (111) and (-111) and tetragonal (101) peaks.

Raman spectroscopy was performed with an XploRA PLUS Raman system equipment (HORIBA) with a CCD detector, an optical microscope (Olympus BX), and solid-state laser (532 nm/25 mW). Fourier transformed infrared spectra (FT-IR) were collected in a Shimadzu IRAffinity-1 spectrophotometer. The powders (<5%wt) were pressed into 100 mg wafers together with KBr (J.T.Baker, Infrared grade).

Diffuse reflectance UV-Vis spectroscopy (UV-Vis/DRS) was carried out on Shimadzu UV-2600 spectrophotometer equipped with an integrating sphere accessory and BaSO_4 as reference (99% reflectance). The band-gap (E_g) values were calculated using Kubelka-Munk function, $F(R)$, by the construction of a Tauc's plot: $(F(R)*hv)^2$ or $(F(R)*hv)^{1/2}$ versus energy (eV), for a direct and indirect allowed transition, respectively. The BET specific surface areas (S_{BET}) and pore volume (BJH method) of the samples were determined by N_2 adsorption-desorption isotherms at 77°K using a Quantachrome Autosorb 3B instrument. Degasification of the samples was performed at 100°C during 12 h. Surface morphology of the materials was analyzed by field emission scanning electron microscopy (FESEM) using a Hitachi S-4800 microscope, whereas high-resolution transmission electron microscopy (HRTEM) was performed in a JEOL JSM-2100 electron microscope operated at 200 kV, with a 0.19 nm resolution.

2.6. Photocatalytic Activity. Synthesized particles were tested in the photodegradation of phenol. The photocatalytic study was carried out in a 250 mL pyrex reactor covered with a UV-transparent Plexiglas (absorption at 250 nm); the intensity of the radiation over the suspension was 90 W/m². For each test, 200 mg of photocatalyst were suspended into 200 mL of phenol solution (50 ppm). The suspension was magnetically stirred in the dark with oxygen flow of 20 L/h until adsorption-desorption equilibrium was reached (ca. 20 min). Then the suspension was illuminated with an Osram Ultra-Vitalux lamp (300 W, UV-A, $\lambda = 365$ nm). Aliquots of 3 mL were taken and filtered (Millipore Milex-HV 0.45 μm) for further analysis. Variations in phenol concentration were tracked by high-performance liquid chromatography (HPLC) using an Agilent Technologies 1200 chromatograph equipped with a UV-Vis detector and Eclipse XDB-C18 column 5 μm , 4.6 mm × 150 mm. The mobile phase was water/methanol (65:35) at a flow rate of 0.8 mL/min. Mineralization of phenol was measured by the total organic content (TOC) in a Shimadzu 5000 TOC analyzer. The percentage of mineralization was estimated using the equation (equation (2)):

$$\% \text{ Mineralization} = 1 - \frac{\text{TOC}_{\text{final}}}{\text{TOC}_{\text{initial}}} * 100, \quad (3)$$

where $\text{TOC}_{\text{initial}}$ and $\text{TOC}_{\text{final}}$ are the total organic carbon concentrations in the media before and after the photocatalytic reaction, respectively.

3. Results

3.1. X-Ray Diffraction Analysis. X-ray patterns of the photocatalysts are depicted in Figure 1(a). All the diffractograms of the samples containing ZnO exhibited sharp and strong peaks at 31.70°, 34.30° y 36.20 (2θ) which correspond to (100), (002), and (101) reflections, respectively, and agree with the characteristic peaks of ZnO wurtzite-type hexagonal crystalline structure (JCPDS 36-1451). The high intensity of the (101) peak suggests anisotropic growth and orientation of the crystals [22, 23].

On the other hand, pristine ZrO_2 showed broad peaks located at 28.20°, 30.20°, and 31.50° (2θ). The peak centered at 30.20°(101) is characteristic of tetragonal crystalline phase ($t\text{-ZrO}_2$) according to JCPDS 79-1771 card, whereas those at 28.20°(-111) and 31.5°(111) are representative of monoclinic phase ($m\text{-ZrO}_2$, JCPDS 37-1484). These results suggest a mixture of both tetragonal and monoclinic crystalline phases, which is commonly observed on ZrO_2 materials when calcined at similar temperatures [24, 25].

When ZnO was added to ZrO_2 , the corresponding peaks to monoclinic phase were not observed, indicating inhibition of monoclinic phase. As the content of ZnO increases, the reflection (101) observed at 30.20° (2θ) appeared slightly shifted towards 30.38° except for the 50 ZnO - ZrO_2 sample; therefore, the peaks observed for all the ZnO - ZrO_2 materials are assigned to the presence of tetragonal phase. To distinguish between the diffraction patterns of cubic and tetragonal phases of ZrO_2 , the 2θ region at 71–77° was carefully examined. The asymmetric doublets at ~74° indicated the formation of tetragonal ZrO_2 [26–28]. Figure 1(b) shows the tetragonal doublets for all ZnO - ZrO_2 materials. Crystallite size and percentage of phases for pure ZnO and ZrO_2 and ZnO - ZrO_2 nanocomposites were determined using Debye-Scherrer equation and Garvie and Nicholson method. Because monoclinic phase was not observed in ZnO - ZrO_2 composites, we considered only the integral intensities of tetragonal and wurtzite peaks of ZrO_2 and ZnO , respectively. The obtained values are presented in Table 1.

3.2. Raman Spectroscopy. The theory of groups predicts six Raman-active modes of vibrations for tetragonal ($A_{1g} + 2B_{1g} + 3E_g$) and 18 for monoclinic ($9A_g + 9B_g$) of ZrO_2 , whereas for ZnO there are 4 Raman-active modes, although splitting of E_2 modes into longitudinal optical (LO) and transversal optical (TO) gives place to 6 active modes. In Figure 2, Raman spectra of the photocatalysts are presented. For ZnO , two peaks can be clearly observed, the first one at 99 cm⁻¹ and the second at 434 cm⁻¹, corresponding to E_2 mode characteristic of wurtzite-type structure; two additional weak bands at 326 and 380 cm⁻¹ were also observed which are related to 2-phonon and $A_1(\text{TO})$ mode,

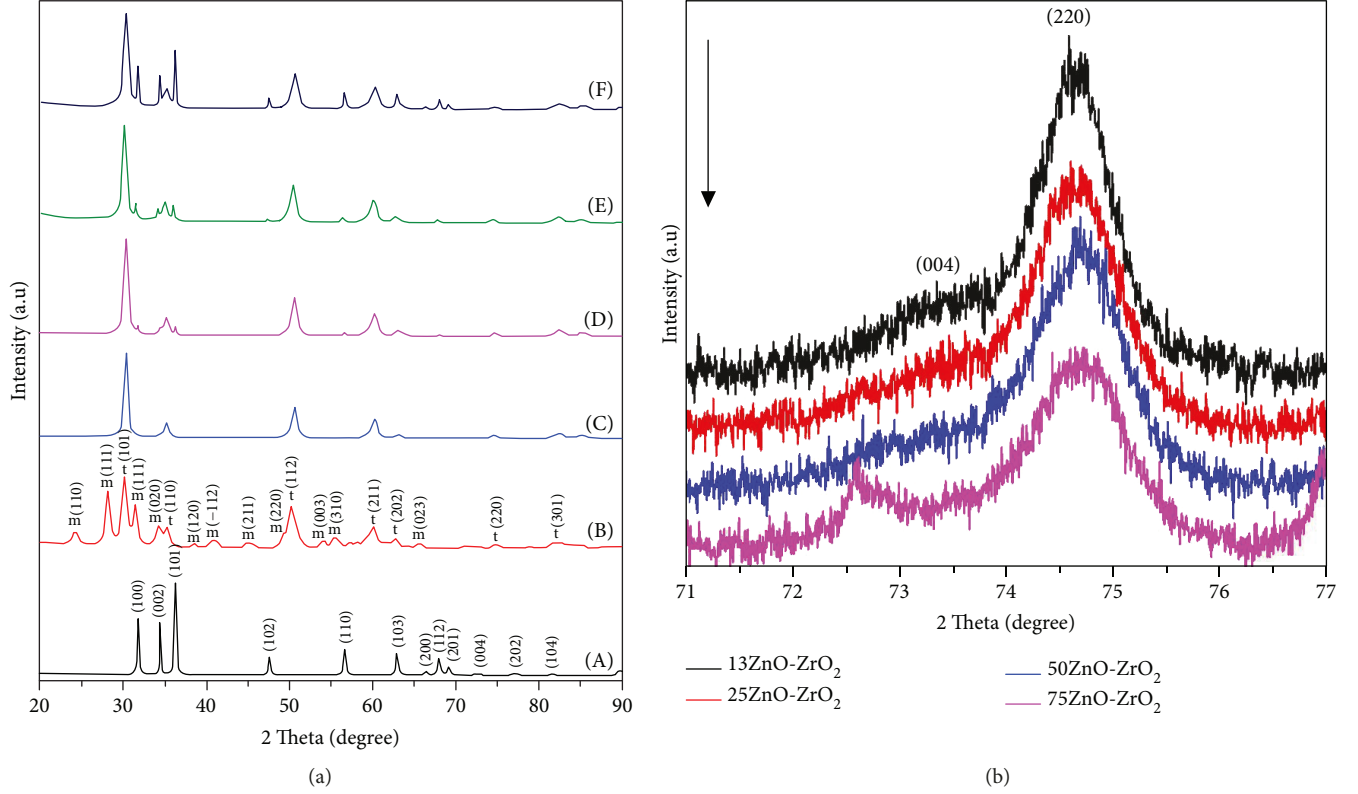


FIGURE 1: (a) XRD pattern of (A) ZnO, (B) ZrO₂, (C) 13ZnO-ZrO₂, (D) 25ZnO-ZrO₂, (E) 50ZnO-ZrO₂, and (E) 75ZnO-ZrO₂ calcined at 500°C. t = tetragonal and m = monoclinic of ZrO₂; w = wurtzite for ZnO. (b) XRD pattern of the samples evaluated in the region of 71–77° to identify the tetragonal doublets of ZrO₂.

TABLE 1: Crystallite size and percentage of phase content of nanocomposites obtained from Debye-Scherrer equation and Garvie and Nicholson method, respectively. m represents monoclinic and t tetragonal phase of ZrO₂. w indicates the wurtzite structure of ZnO.

Sample	Crystallite size (nm)	<i>h k l</i>	Phase content (%)
ZnO	33.2	(101)	100%
ZrO ₂	14.3	(101) _m	59.7%
	15.4	(-111) _t	40.3%
13ZnO-ZrO ₂	18.2	(101) _t	100%
	—	—	—
25ZnO-ZrO ₂	14.5	(101) _t	88.0%
	44.7	(101) _w	12.0%
50ZnO-ZrO ₂	14.4	(101) _t	82.0%
	48.3	(101) _w	18.0%
75ZnO-ZrO ₂	13.8	(101) _t	60.9%
	44.6	(101) _w	39.1%

respectively [29]. The ZrO₂ spectrum showed several peaks located at 100, 176, 217, 306, 333, 380, 474, 501, 534, 553, 613, and 638 cm⁻¹, which are very close to those reported for monoclinic phase. The peaks attributed to tetragonal structure were located at 142 and 265 cm⁻¹ whereas two additional bands reported for this structure around 318 and 461 cm⁻¹ seemed to be overlapped with monoclinic signals;

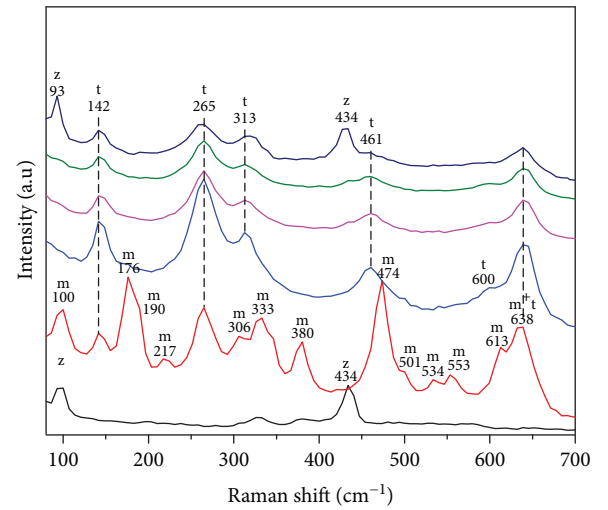


FIGURE 2: Raman spectra of ZnO-ZrO₂ nanocomposites. (A) ZnO, (B) ZrO₂, (C) 13ZnO-ZrO₂, (D) 25ZnO-ZrO₂, (E) 50ZnO-ZrO₂, and (F) 75ZnO-ZrO₂. m indicates monoclinic and t tetragonal structures for ZrO₂ whereas z indicates wurtzite crystalline structure of ZnO.

the peaks between 640 and 641 cm⁻¹ are shared by monoclinic and tetragonal structures [30, 31]. Since cubic structure of zirconia usually exhibits one strong peak around 617 cm⁻¹, the absence of this signal indicates the presence of a mixture of only two structures (monoclinic and tetragonal) in pristine

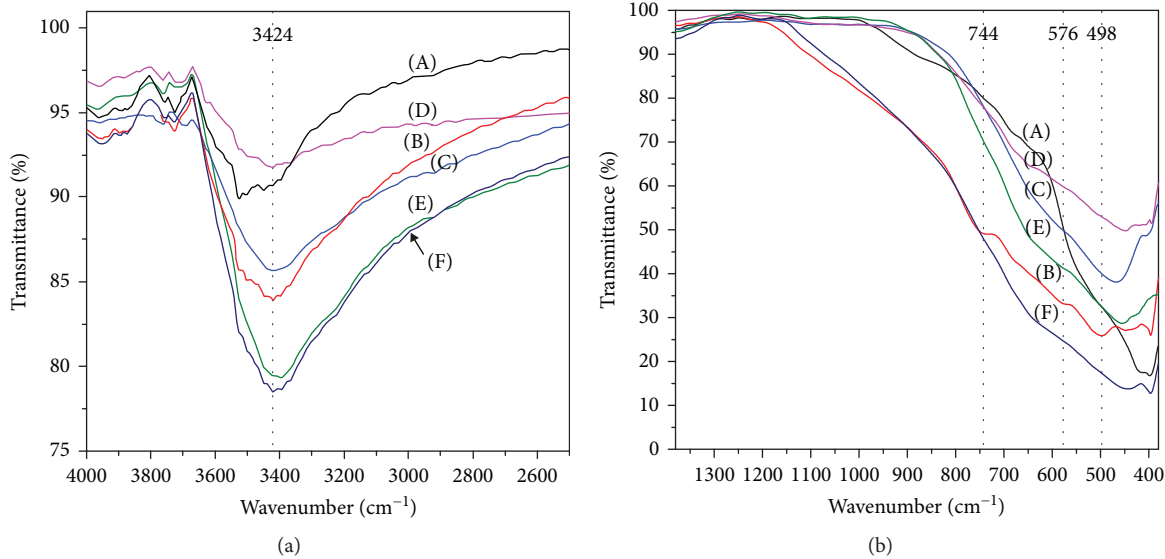


FIGURE 3: (a) FT-IR full spectra of (A) ZnO, (B) ZrO₂, (C) 13ZnO-ZrO₂, (D) 25ZnO-ZrO₂, (E) 50ZnO-ZrO₂, and (F) 75ZnO-ZrO₂ composites with different content of ZnO. (b) FTIR region from 1300 to 400 cm⁻¹.

ZrO₂. For the ZnO-ZrO₂ composites, Raman spectra did not show sharp peaks. As the content of ZnO increased, we observed the broadening of the peaks that correspond to tetragonal structure modes; this broadening is related to the decrease in the crystallite size of this crystalline phase, usually due to phonons associated with the nanosized particles. On the other hand, the absence of representative signals for monoclinic structure in both Raman spectra and XRD patterns leads us to conclude that ZnO inhibited the formation of this structure in ZnO-ZrO₂ composites. Additionally, Rietveld refinement of 13ZnO-ZrO₂ was performed (Supplementary Materials, Figure S4 and Table S1). This analysis confirmed the absence of both solid solution and cubic crystalline phase formation; the estimated percentages of each crystalline structure are shown in Table 1.

3.3. FTIR Analysis. Figure 3 shows the spectra of pure ZnO, ZrO₂, and ZnO-ZrO₂ composites with different content of ZnO. FTIR spectra of all materials presented wide bands at 3410–3450 cm⁻¹ which correspond to O-H stretching vibrations of physical adsorbed water on the catalyst surface [32]. Compared to the ZrO₂ band, a shift of the O-H band to lower frequencies occurs as the percentage of ZnO increases in the ZnO-ZrO₂ composites. Pure ZnO spectrum showed an intense band centered at 423 cm⁻¹. This band is characteristic for Zn-O vibrations [23, 32]. Two intense bands appeared at 744 cm⁻¹ and 576 cm⁻¹ have been associated with vibrations of Zr-O in monoclinic structure. An additional band located at 498 cm⁻¹ was also present in ZrO₂ spectrum; this signal corresponds to Zr-O-Zr vibrations in tetragonal structure [33–35], which appears slightly shifted for all ZnO-ZrO₂ nanocomposites. This behavior can be attributed to the addition of divalent oxides like ZnO (Zn²⁺) to ZrO₂. Also, the incorporation of these oxides may produce a lattice deformation on the crystalline structure, with subsequent modification on the force constants of Zr-O and related bonds [33].

3.4. Specific Surface Area. Figure 4 shows the N₂ adsorption-desorption isotherms of the nanocomposites as well as their corresponding pore size distribution (insets). The isotherms for all the samples presented type IV(a) shape according to IUPAC classification [36] which corresponds to mesoporous structures where capillary condensation takes place and is accompanied by hysteresis. The adsorbed volume in all cases is relatively low which explains the observed values for specific surface area. It has been reported that ZnO usually exhibits poor BET surface areas ranging from 1 to 15 m²/g when no additives are used to improve this property. In our samples, pure ZnO showed a S_{BET} = 10 m²/g while ZrO₂ exhibited 46 m²/g.

The isotherms of both ZnO and ZrO₂ pure oxides showed a narrow hysteresis loop, which for ZrO₂ starts at 0.4 (P/P₀) and for ZnO this occurs at higher relative pressures (0.8) (Figure 4(a)). When composites were analyzed, hysteresis loop for all the composition was slightly broader than pure oxides, indicating changes in porosity (Figure 4(b)). ZnO showed H3-type hysteresis loop at high relative pressure. However, ZrO₂ and all ZnO-ZrO₂ composites exhibited H2-type hysteresis which is associated with the presence of bottle-shaped mesopores that can be explained as a consequence of the interconnectivity of pores [1]. The specific surface area decreased from 46 to 8 m²/g when 25% of ZnO was incorporated, and for 75ZnO-ZrO₂, S_{BET} value was 36 m²/g, and its N₂ isotherm showed a broader hysteresis loop than the observed pure oxides. Additional effect of ZnO incorporation was observed in BJH pore size distribution: pristine ZrO₂ showed a wide pore size distribution from meso- to macropores, whereas ZnO presented pores around 30 nm and also macroporosity; when both oxides were coupled, pore size distribution for all composites showed unimodal distribution with very close pore size average.

3.5. Diffuse Reflectance UV-Vis Spectroscopy. The absorption spectra of the oxides are depicted in Figure 5(a). The UV-Vis

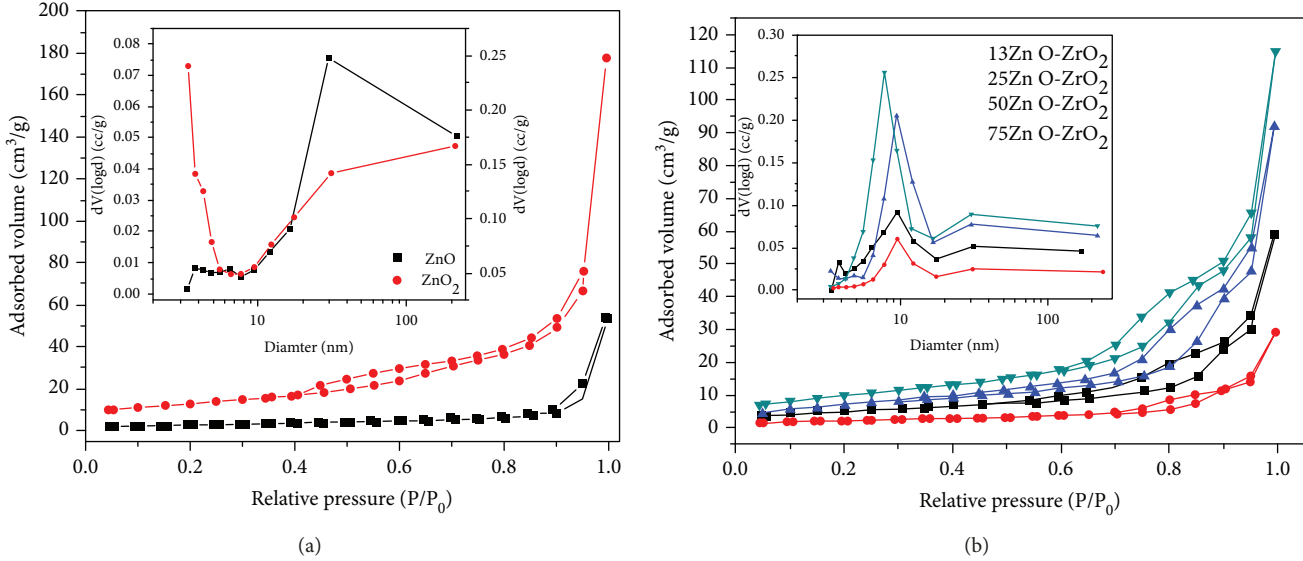


FIGURE 4: N₂ adsorption-desorption BET isotherms of (a) pure oxides and (b) different ZnO-ZrO₂ composites; the insets represent BJH pore size distribution from desorption branches.

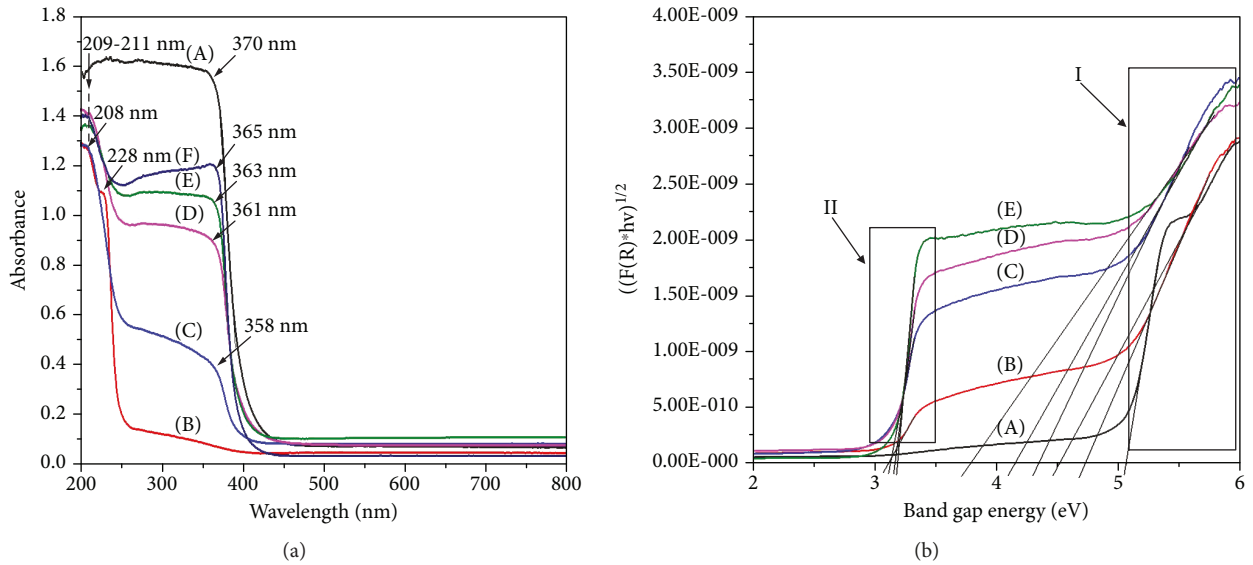


FIGURE 5: (a) UV-Vis/DR absorption spectra of (A) ZnO, (B) ZrO₂, (C) 13ZnO-ZrO₂, (D) 25ZnO-ZrO₂, (E) 50ZnO-ZrO₂, and (F) 75ZnO-ZrO₂ composites; (b) Kubelka-Munk function of (A) ZrO₂, (B) 13ZnO-ZrO₂, (C) 25ZnO-ZrO₂, (D) 50ZnO-ZrO₂, and (E) 75ZnO-ZrO₂ composites. (I) represents the first and (II) the second edge of the samples considered for Eg estimations.

spectrum of ZnO shows an absorption edge at 370 nm, which is in good agreement with literature [37]. This characteristic band can be assigned to the intrinsic band-gap absorption of ZnO due to the electron transitions from the valence band to the conduction band (O2p → Zn3d) [38]. ZrO₂ spectrum showed a small absorption band at 208 nm and another large band at 228 nm, which appeared at lower wavelengths than the characteristic bands reported for ZrO₂, usually observed ~240 nm [39]. These bands correspond to the presence of Zr species as the tetrahedral Zr⁴⁺, and it is electronically produced by the charge transfer transition of the valence band O2p electron to the conduction band Zr4d (O₂ → Zr⁴⁺) level

upon UV light excitation [40]. There was no other absorption band observed in the UV-Vis region. It has been reported that the identification of ZrO₂ phases can be possible by using UV range of DRS. The two bands observed in pure ZrO₂ are typically observed since ZrO₂ has two band-to-band transitions. According to Sahu and Rao [41], the first transition corresponds to values around 5.17–5.2 eV that can be associated with m-ZrO₂. In the ZrO₂ here prepared, we observed by DRX that monoclinic and tetragonal phases are presented in pure oxide. The band at high energy cannot be observed when the content of ZnO increases, not only due to the disappearance of monoclinic phase but also for the

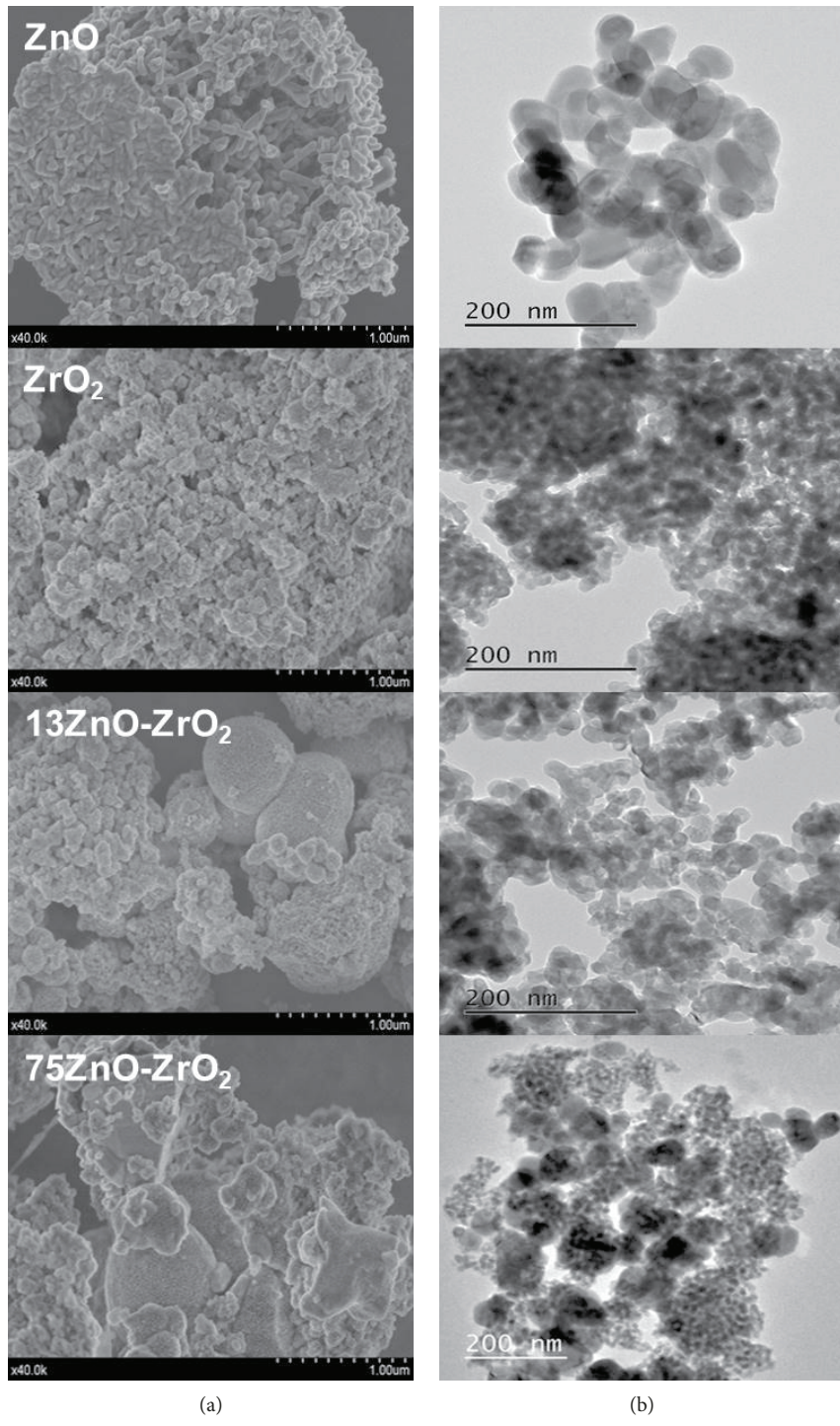


FIGURE 6: FESEM (a) and the corresponding HRTEM (b) micrographs of pure oxides and ZnO-ZrO₂ composites.

incorporation of ZnO affecting the shape of the spectrum. The spectrum of pure ZrO_2 also depicts a small shoulder with an onset at 310 nm that can be attributed to t- ZrO_2 crystalline structure [42]. The shape as well as the intensity of this band changes as the content of ZnO increases and slightly shifts towards lower energy region, due to the effect of ZnO.

The addition of ZnO modified the absorption edge of ZrO_2 towards lower values. A red shift was observed in the last band of all ZnO-ZrO_2 materials towards longer

wavelength region, due to the introduction of energy levels in the interband gap [17]. Kubelka-Munk function was used to estimate the band gap of the nanocomposites (Figure 5(b)). The band gap values of pure ZnO and ZrO_2 were evaluated by using $n = 2$ (direct transitions) and $n = 1/2$ (indirect transitions), respectively, and their values are summarized in Table S2 (Supplementary Materials).

For ZnO-ZrO₂ materials, it can be noticed the presence of two edges instead of only one; the bandgap was estimated

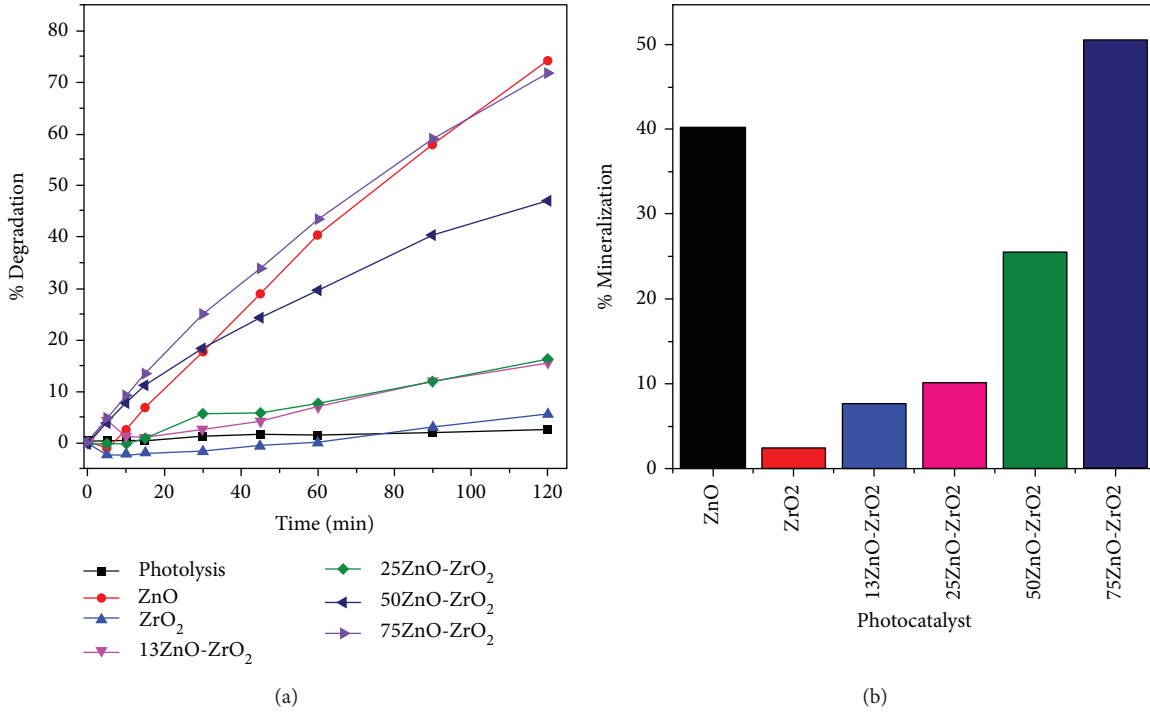


FIGURE 7: (a) Degradation curves of phenol by ZnO, ZrO₂, and different ZnO-ZrO₂ composites (experimental conditions: phenol = 50 ppm, volume of phenol = 200 mL, and catalyst dosage = 200 mg). (b) TOC results obtained after 120 min of illumination in the UV.

using $n = 1/2$. The obtained value for ZnO was 3.26 eV (Supplementary Materials, Figure S5) whereas 4.53 and 5.06 eV were calculated for ZrO₂ (for the two edges observed in the corresponding spectrum), these values changed to 4.73, 4.35, 3.76, and 4.16 eV by the addition of different contents of ZnO (indicated as I in Figure 5(b)), being 50ZnO-ZrO₂ the one with the lowest value. With regard to the low-energy shoulder observed in ZnO-ZrO₂ spectra (indicated as II in Figure 5(b)), the calculated values were 3.07, 3.10, 3.15, and 3.16 eV for the composites with 13, 25, 50, and 75% of ZnO, respectively, allowing nanocomposites to be excited at lower energy.

3.6. Electron Microscopy. Morphology of the nanocomposites was investigated using electron microscopy, and the images are shown in Figure 6. We observed that ZnO nanoparticles are rod-like shaped with sizes ranging from 100 to 300 nm producing agglomerates. On the other hand, ZrO₂ is made of smaller particles nonuniform in shape and size. In 13ZnO-ZrO₂ nanocomposite, we observed that ZnO particles change in shape whereas some ZrO₂ agglomerates grew up to 1 μ m but also smaller quasispherical particles around 300 nm were observed. The most significant change was exhibited by 75ZnO-ZrO₂ nanocomposite, since agglomerates of particles with smaller sizes were obtained.

3.7. Photocatalytic Test. Previous to the test, adsorption-desorption equilibrium was reached after stirring the suspensions for 20 minutes in the dark, of which in general all the composites presented low adsorption of the pollutant. The results of photocatalytic degradation are shown in

TABLE 2: Kinetic parameters estimated from pseudofirst order kinetics.

Photocatalyst	k (min ⁻¹)	R ²	t _{1/2} (min)
ZrO ₂	0.7×10^{-3}	0.9585	1155
13ZnO-ZrO ₂	1.3×10^{-3}	0.9193	533
25ZnO-ZrO ₂	1.5×10^{-3}	0.9808	462
50ZnO-ZrO ₂	5.3×10^{-3}	0.9939	130
75ZnO-ZrO ₂	10.3×10^{-3}	0.9964	67
ZnO	11.2×10^{-3}	0.9810	62

Figure 7(a). Here, we observed that pure ZrO₂ degraded only 5% of phenol even after 120 min; when ZnO was incorporated, a slight increase in photodegradation with 13 and 25% of ZnO was observed, but they barely degraded around 15% of the pollutant. By increasing the ZnO content up to 50 mol, 47% of phenol was degraded, whereas 71% of degradation was achieved using 75ZnO-ZrO₂ composite. For the prepared ZnO, 74% of degradation was obtained during the same time. The kinetic parameters were also calculated assuming pseudofirst order kinetics (Table 2) where we observed that t_{1/2} for 75ZnO-ZrO₂ composite was very close to that calculated for ZnO.

It is well known that ZnO can be activated under UV-A light and generally exhibits good photodegradation rates, but it is also needed to assess the mineralization of the pollutant. For this purpose, TOC analysis was performed and the results are tabulated in Figure 7(b). Pure ZrO₂

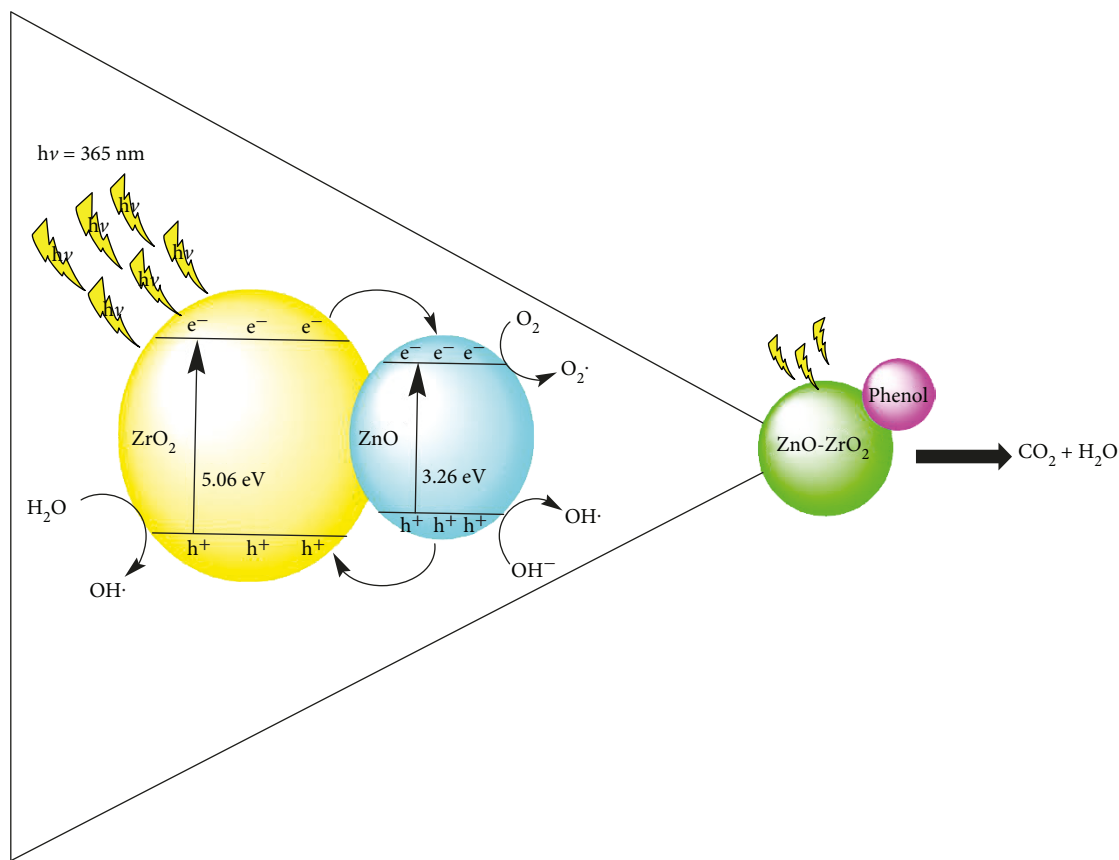


FIGURE 8: Schematic representation of photocatalytic mechanism of electron-hole pair separation of ZnO-ZrO₂ composites for the degradation of phenol.

mineralized 2.5% of phenol, but the mineralization increases with increasing ZnO content, which stabilizes tetragonal crystalline phases of ZrO₂. Although ZnO reached 74% degradation, the mineralization of the pollutant was 40%, while 51% of mineralization was achieved with 75ZnOZrO₂. Tetragonal ZrO₂ has been reported as the most active polymorph of ZrO₂ which also shows high selectivity in catalytic reactions. These results showed that at this concentration, ZnO-ZrO₂ composite improved the mineralization of phenol when compared to pure ZnO. Besides, it was also confirmed that intermediaries like catechol, resorcinol, and hydroquinone were not generated during the photodegradation with 75ZnO-ZrO₂.

According to the obtained results, a schematic representation of phenol degradation is shown in Figure 8. When the ZnO-ZrO₂ composites were excited by Uv-A irradiation (365 nm), electrons migrate from the valence band (VB) to the conduction band (CB) of ZnO, leading to the formation of electron/hole (e⁻/h⁺) pairs. Since the energy levels of ZnO fit well into the band gap of ZrO₂, the electrons from the CB of ZrO₂ can easily be transferred to the CB of ZnO; conversely, the holes migrate from the VB of ZnO to the VB of ZrO₂, and thereby the electron-hole pair recombination may be decreased in ZnO-ZrO₂ composites. These e⁻ and h⁺ react with water and oxygen to produce hydroxyl (OH⁻) radicals which are very reactive and can easily oxidize

the phenol until obtaining CO₂ and water. As a result, we obtained an enhancement in photocatalytic performance of phenol degradation by the composite with the highest ZnO percentage [8, 19, 20, 43].

4. Discussion

It is well known that the catalytic and photocatalytic performance of ZrO₂ can be affected by crystalline phases. Although there are some reports on the catalytic activity of ZnO-ZrO₂ materials, deep structural studies have not been performed so far. The fact that both tetragonal and cubic phases exhibit similar XRD patterns makes it difficult to discern these structures based only on X-ray diffraction analysis, and Rietveld refinement or Raman spectroscopy are good tools for elucidating this ambiguity. In this work, we observed that by adding ZnO, only the t-ZrO₂ phase was obtained, and this phenomenon could also be suspected by analyzing Raman results. In all composites, t-ZrO₂ was detected as well as zincite (wurtzite-type) structure for ZnO. Formation of the nanocomposite influenced the crystallite size of both ZnO and ZrO₂, increasing for ZnO but decreasing for t-ZrO₂ as a function of the ZnO-ZrO₂ ratio. The absence of solid solution could be explained not only due to the differences in valence between ions, which depends on the amount of Zn²⁺ species [44], but also due to the synthesis procedure

here reported. Lattice parameters of the $13\text{ZnO}\text{ZrO}_2$ nanocomposite are provided in Supplementary Materials. We observed small changes when compared to pure zirconia; this can be attributed to the presence of the divalent oxide, since incorporation of these type of oxides causes lattice deformation on the crystalline structure of ZrO_2 , with subsequent modification on the force constants of Zr-O and related bonds [33].

Since band gap is one important feature to consider in photoactivity, many attempts to improve this property have been made. By coupling ZnO and ZrO_2 , radiation of low energy can be absorbed by the ZnO-ZrO_2 composites. From the calculated E_g values, it can be assumed that the energy levels for both the valence band (VB) and conduction band (CB) in ZnO fit in with the bandgap of ZrO_2 . When the electrons are excited, most of the electrons from the conduction band of ZrO_2 can be easily transferred to the conduction band of ZnO , and thus, the band gap may be decreased, indicating that ZnO-ZrO_2 nanoparticles have a suitable band gap to generate excited electron/hole pairs [17] allowing the use of simulated solar radiation.

Both oxides, ZnO and ZrO_2 , are well known for their photocatalytic properties, but one of their limitations is the need of UV light for its activation, especially ZrO_2 that usually requires UV radiation due to its wide band gap. Here, we investigated the effect of ZnO in the photocatalytic performance of ZrO_2 under simulated solar light. Since the use of pure ZnO leads to the formation of several compounds during the photoreaction, it is remarkable that 75ZnO-ZrO_2 nanocomposite conducted to a reaction without formation of any intermediaries, which represents the main advantage of using ZnO-ZrO_2 .

5. Conclusions

So far, ZnO-ZrO_2 materials have been reported for several catalytic reactions with an enhanced performance compared to their pristine moieties. Recently, this type of composites has been studied also as photocatalysts with promising results, but full understanding of their properties related to their composition are needed. In this work, we prepared ZnO-ZrO_2 composites using zinc (II) acetylacetone and zirconium n-butoxide as raw materials. We observed that synthesis procedure strongly affected the stabilization of zirconia polymorphs, where ZnO plays an important role in inhibiting ZrO_2 monoclinic structure and stabilizing tetragonal phase. By coupling ZnO to ZrO_2 , we observed significant changes in the absorption behavior of ZrO_2 shifting its absorption edges in the UV region toward lower energies. The pore distribution of the composite was intensely changed by the interaction of both oxides, directing to a larger amount of mesopores than the observed for uncoupled oxides. Test revealed that 75ZnO-ZrO_2 composite exhibited good performance in the degradation of phenol using simulated solar radiation, improved the mineralization reached by pure ZnO and ZrO_2 , and inhibited the formation of undesirable intermediates usually obtained as a result of photocatalytic degradation of phenol.

Data Availability

All data obtained from characterizations techniques used to support this study are available from the corresponding author upon request.

Conflicts of Interest

The authors declare that they have no conflicts of interest.

Acknowledgments

We are grateful to D.H. Aguilar and A. Marín for their technical assistance, and acknowledge the financial support of the projects UJAT-IB-43, CONACYT-INFR-269701, SEP-CONACYT-CB-183196, FOMIX-Yucatán 2008-108160, and CONACYT LAB-2009-01 (No. 123913). In addition, we would like to thank CONACYT for the fellowship given to M. Uribe, and to ICMS-CSIC, LANNBIO CINVESTAV-Mérida, UAM-I, and UJAT for the facilities.

Supplementary Materials

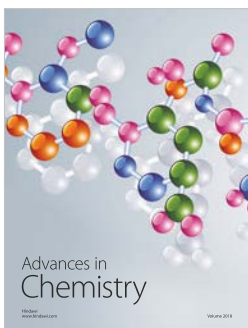
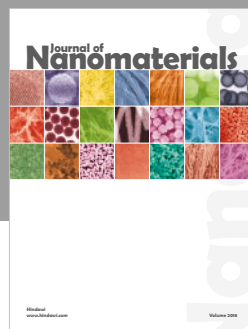
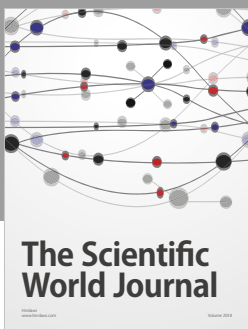
In the supplementary information, the authors provided the details on the mechanism of formation for ZnO-ZrO_2 materials, as well as the crystalline data obtained through the Rietveld refinement and HRTEM of the $13\text{ZnO}\text{ZrO}_2$. (*Supplementary Materials*)

References

- [1] B. Sathyaseelan, E. Manikandan, I. Baskaran et al., "Studies on structural and optical properties of ZrO_2 nanopowder for opto-electronic applications," *Journal of Alloys and Compounds*, vol. 694, pp. 556–559, 2017.
- [2] C. Karunakaran, R. Dhanalakshmi, and P. Gomathisankar, "Phenol-photodegradation on ZrO_2 . Enhancement by semiconductors," *Spectrochimica Acta Part A: Molecular and Biomolecular Spectroscopy*, vol. 92, pp. 201–206, 2012.
- [3] A. M. Hussein and R. V. Shende, "Enhanced hydrogen generation using ZrO_2 -modified coupled ZnO/TiO_2 nanocomposites in the absence of noble metal co-catalyst," *International Journal of Hydrogen Energy*, vol. 39, no. 11, pp. 5557–5568, 2014.
- [4] S. Aghabeygi and M. Khademi-Shamami, " ZnO/ZrO_2 nanocomposite: sonosynthesis, characterization and its application for wastewater treatment," *Ultrasonics Sonochemistry*, vol. 41, pp. 458–465, 2018.
- [5] C. Karunakaran, R. Dhanalakshmi, P. Gomathisankar, and G. Manikandan, "Enhanced phenol-photodegradation by particulate semiconductor mixtures: interparticle electron-jump," *Journal of Hazardous Materials*, vol. 176, no. 1-3, pp. 799–806, 2010.
- [6] A. Shirmardi, M. A. M. Teridi, H. R. Azimi, W. J. Basirun, F. Jamali-Sheini, and R. Yousefi, "Enhanced photocatalytic performance of ZnSe/PANI nanocomposites for degradation of organic and inorganic pollutants," *Applied Surface Science*, vol. 462, pp. 730–738, 2018.
- [7] L. J. Tomar and B. S. Chakrabarty, "Synthesis, structural and optical properties of $\text{TiO}_2\text{-ZrO}_2$ nanocomposite by

- hydrothermal method," *Advanced Materials Letters*, vol. 4, no. 1, pp. 64–67, 2013.
- [8] B. M. Pirzada, N. A. Mir, N. Qutub, O. Mehraj, S. Sabir, and M. Muneer, "Synthesis, characterization and optimization of photocatalytic activity of TiO_2/ZrO_2 nanocomposite heterostructures," *Materials Science and Engineering: B*, vol. 193, pp. 137–145, 2015.
- [9] R. Yousefi, J. Beheshtian, S. M. Seyed-Talebi, H. R. Azimi, and F. Jamali-Sheini, "Experimental and theoretical study of enhanced photocatalytic activity of Mg-doped ZnO NPs and ZnO/rGO nanocomposites," *Chemistry - An Asian Journal*, vol. 13, no. 2, pp. 194–203, 2018.
- [10] C. Jaramillo-Páez, J. A. Navío, M. C. Hidalgo, and M. Macías, "High UV-photocatalytic activity of ZnO and Ag/ZnO synthesized by a facile method," *Catalysis Today*, vol. 284, pp. 121–128, 2017.
- [11] A. C. Mohan and B. Renjanadevi, "Preparation of zinc oxide nanoparticles and its characterization using scanning electron microscopy (SEM) and X-ray diffraction(XRD)," *Procedia Technology*, vol. 24, pp. 761–766, 2016.
- [12] G. Kavitha, K. T. Arul, and P. Babu, "Enhanced acetone gas sensing behavior of n-ZnO/p-NiO nanostructures," *Journal of Materials Science: Materials in Electronics*, vol. 29, no. 8, pp. 6666–6671, 2018.
- [13] A. Kharatzadeh, F. Jamali-Sheini, and R. Yousefi, "Excellent photocatalytic performance of $Zn(1-x)MgxO/rGO$ nanocomposites under natural sunlight irradiation and their photovoltaic and UV detector applications," *Materials & Design*, vol. 107, pp. 47–55, 2016.
- [14] P. Prasannalakshmi and N. Shanmugam, "Fabrication of TiO_2/ZnO nanocomposites for solar energy driven photocatalysis," *Materials Science in Semiconductor Processing*, vol. 61, pp. 114–124, 2017.
- [15] G. S. Pozan and A. Kambur, "Significant enhancement of photocatalytic activity over bifunctional $ZnO-TiO_2$ catalysts for 4-chlorophenol degradation," *Chemosphere*, vol. 105, pp. 152–159, 2014.
- [16] N. Rosman, W. N. W. Salleh, A. F. Ismail et al., "Photocatalytic degradation of phenol over visible light active $ZnO/Ag_2CO_3/Ag_2O$ nanocomposites heterojunction," *Journal of Photochemistry and Photobiology A: Chemistry*, vol. 364, pp. 602–612, 2018.
- [17] M. M. Ibrahim, "Photocatalytic activity of nanostructured $ZnO-ZrO_2$ binary oxide using fluorometric method," *Spectrochimica Acta Part A: Molecular and Biomolecular Spectroscopy*, vol. 145, pp. 487–492, 2015.
- [18] G. C. Lakshmi, S. Ananda, R. Somashekhar, and C. Ranganathaiah, "Synthesis of ZnO/ZrO_2 nanocomposites by electrochemical method and photocatalytic degradation of fast green dye, paper dyeing and printing press effluent," *International Journal of Advanced Materials Science*, vol. 3, no. 3, pp. 221–237, 2012.
- [19] E. D. Sherly, J. J. Vijaya, N. C. S. Selvam, and L. J. Kennedy, "Microwave assisted combustion synthesis of coupled $ZnO-ZrO_2$ nanoparticles and their role in the photocatalytic degradation of 2,4-dichlorophenol," *Ceramics International*, vol. 40, no. 4, pp. 5681–5691, 2014.
- [20] K. Gurushantha, L. Renuka, K. S. Anantharaju et al., "Photocatalytic and photoluminescence studies of ZrO_2/ZnO nanocomposite for LED and waste water treatment applications," *Materials Today: Proceedings*, vol. 4, no. 11, Part 3, pp. 11747–11755, 2017.
- [21] R. C. Garvie and P. S. Nicholson, "Phase analysis in zirconia systems," *Journal of the American Ceramic Society*, vol. 55, no. 6, pp. 303–305, 1972.
- [22] Y. Peng, J. Ji, X. Zhao, H. Wan, and D. Chen, "Preparation of ZnO nanopowder by a novel ultrasound assisted non-hydrolytic sol-gel process and its application in photocatalytic degradation of C.I. Acid Red 249," *Powder Technology*, vol. 233, pp. 325–330, 2013.
- [23] M. M. Ba-Abbad, A. A. H. Kadhum, A. Bakar Mohamad, M. S. Takriff, and K. Sopian, "The effect of process parameters on the size of ZnO nanoparticles synthesized via the sol-gel technique," *Journal of Alloys and Compounds*, vol. 550, pp. 63–70, 2013.
- [24] F. Heshmatpour and R. B. Aghakhanpour, "Synthesis and characterization of nanocrystalline zirconia powder by simple sol-gel method with glucose and fructose as organic additives," *Powder Technology*, vol. 205, no. 1-3, pp. 193–200, 2011.
- [25] A. K. Singh and U. T. Nakate, "Microwave synthesis, characterization, and photoluminescence properties of nanocrystalline zirconia," *The Scientific World Journal*, vol. 2014, Article ID 349457, 7 pages, 2014.
- [26] C. Wang, M. Boucher, M. Yang, H. Saltsburg, and M. Flytzani-Stephanopoulos, "ZnO-modified zirconia as gold catalyst support for the low-temperature methanol steam reforming reaction," *Applied Catalysis B: Environmental*, vol. 154–155, pp. 142–152, 2014.
- [27] R. Srinivasan, R. J. de Angelis, G. Ice, and B. H. Davis, "Identification of tetragonal and cubic structures of zirconia using synchrotron x-radiation source," *Journal of Materials Research*, vol. 6, no. 6, pp. 1287–1292, 1991.
- [28] R. C. Garvie, R. H. Hannink, and R. T. Pascoe, "Ceramic steel?," *Nature*, vol. 258, no. 5537, pp. 703–704, 1975.
- [29] S. K. Sharma and G. J. Exarhos, "Raman spectroscopic investigation of ZnO and doped ZnO films, nanoparticles and bulk material at ambient and high pressures," *Solid State Phenomena*, vol. 55, pp. 32–37, 1997.
- [30] D. Gazzoli, G. Mattei, and M. Valigi, "Raman and X-ray investigations of the incorporation of Ca^{2+} and Cd^{2+} in the ZrO_2 structure," *Journal of Raman Spectroscopy*, vol. 38, no. 7, pp. 824–831, 2007.
- [31] V. G. Keramidas and W. B. White, "Raman scattering study of the crystallization and phase transformations of ZrO_2 ," *Journal of the American Ceramic Society*, vol. 57, no. 1, pp. 22–24, 1974.
- [32] T. Ivanova, A. Harizanova, T. Koutzarova, and B. Vertruyen, "Effect of annealing temperatures on properties of sol-gel grown $ZnO-ZrO_2$ films," *Crystal Research and Technology*, vol. 45, no. 11, pp. 1154–1160, 2010.
- [33] J. Chandradass, K.-S. Han, and D. Bae, "Synthesis and characterization of zirconia- and silica-doped zirconia nanopowders by oxalate processing," *Journal of Materials Processing Technology*, vol. 206, no. 1–3, pp. 315–321, 2008.
- [34] E. S. Agorku, A. T. Kuvarega, B. B. Mamba, A. C. Pandey, and A. K. Mishra, "Enhanced visible-light photocatalytic activity of multi-elements-doped ZrO_2 for degradation of indigo carmine," *Journal of Rare Earths*, vol. 33, no. 5, pp. 498–506, 2015.
- [35] H. Sudrajat, S. Babel, H. Sakai, and S. Takizawa, "Rapid enhanced photocatalytic degradation of dyes using novel N-doped ZrO_2 ," *Journal of Environmental Management*, vol. 165, pp. 224–234, 2016.

- [36] M. Thommes, K. Kaneko, A. V. Neimark et al., "Physisorption of gases, with special reference to the evaluation of surface area and pore size distribution (IUPAC Technical Report)," *Pure and Applied Chemistry*, vol. 87, no. 9-10, pp. 1051–1069, 2015.
- [37] X. Zhao, M. Li, and X. Lou, "Sol-gel assisted hydrothermal synthesis of ZnO microstructures: morphology control and photocatalytic activity," *Advanced Powder Technology*, vol. 25, no. 1, pp. 372–378, 2014.
- [38] A. K. Zak, M. E. Abrishami, W. H. A. Majid, R. Yousefi, and S. M. Hosseini, "Effects of annealing temperature on some structural and optical properties of ZnO nanoparticles prepared by a modified sol-gel combustion method," *Ceramics International*, vol. 37, no. 1, pp. 393–398, 2011.
- [39] K. G. Kanade, J. O. Baeg, S. K. Apte, T. L. Prakash, and B. B. Kale, "Synthesis and characterization of nanocrystalline zirconia by hydrothermal method," *Materials Research Bulletin*, vol. 43, no. 3, pp. 723–729, 2008.
- [40] T. Sreethawong, S. Ngamsinlapasathian, and S. Yoshikawa, "Synthesis of crystalline mesoporous-assembled ZrO₂ nanoparticles via a facile surfactant-aided sol-gel process and their photocatalytic dye degradation activity," *Chemical Engineering Journal*, vol. 228, pp. 256–262, 2013.
- [41] H. Ranjan Sahu and G. Ranga Rao, "Characterization of combustion synthesized zirconia powder by UV-Vis, IR and other techniques," *Bulletin of Materials Science*, vol. 23, no. 5, pp. 349–354, 2000.
- [42] S. N. Basahel, T. T. Ali, M. Mokhtar, and K. Narasimharao, "Influence of crystal structure of nanosized ZrO₂ on photocatalytic degradation of methyl orange," *Nanoscale Research Letters*, vol. 10, no. 1, p. 73, 2015.
- [43] S. Sultana, Rafiuddin, M. Z. Khan, and M. Shahadat, "Development of ZnO and ZrO₂ nanoparticles: their photocatalytic and bactericidal activity," *Journal of Environmental Chemical Engineering*, vol. 3, no. 2, pp. 886–891, 2015.
- [44] G. Štefanić, S. Musić, and M. Ivanda, "Phase development of the ZrO₂-ZnO system during the thermal treatments of amorphous precursors," *Journal of Molecular Structure*, vol. 924–926, pp. 225–234, 2009.



Hindawi

Submit your manuscripts at
www.hindawi.com

